J. Fluid Mech. (1995), *vol.* 292, *pp.* 95–110

The motion of long bubbles in polygonal capillaries. Part 2. Drag, fluid pressure and fluid flow

By HARRIS WONG,[1]† C. J. RADKE[2] AND S. MORRIS[1]

[1] Department of Mechanical Engineering, University of California, Berkeley, CA 94720, USA

[2] Earth Sciences Division of Lawrence Berkeley Laboratory and Department of Chemical Engineering, University of California, Berkeley, CA 94720, USA

(Received 22 January 1993 and in revised form 26 September 1994)

This work determines the pressure–velocity relation of bubble flow in polygonal capillaries. The liquid pressure drop needed to drive a long bubble at a given velocity U is solved by an integral method. In this method, the pressure drop is shown to balance the drag of the bubble, which is determined by the films at the two ends of the bubble. Using the liquid-film results of Part 1 (Wong, Radke & Morris 1995), we find that the drag scales as $Ca^{2/3}$ in the limit $Ca \to 0$ ($Ca \equiv \mu U/\sigma$, where μ is the liquid viscosity and σ the surface tension). Thus, the pressure drop also scales as $Ca^{2/3}$. The proportionality constant for six different polygonal capillaries is roughly the same and is about a third that for the circular capillary.

The liquid in a polygonal capillary flows by pushing the bubble (plug flow) and by bypassing the bubble through corner channels (corner flow). The resistance to the plug flow comes mainly from the drag of the bubble. Thus, the plug flow obeys the nonlinear pressure–velocity relation of the bubble. Corner flow, however, is chiefly unidirectional because the bubble is long. The ratio of plug to corner flow varies with liquid flow rate Q (made dimensionless by $\sigma a^2/\mu$, where a is the radius of the largest inscribed sphere). The two flows are equal at a critical flow rate Q_c, whose value depends strongly on capillary geometry and bubble length. For the six polygonal capillaries studied, $Q_c \ll 10^{-6}$. For $Q_c \ll Q \ll 1$, the plug flow dominates, and the gradient in liquid pressure varies with $Q^{2/3}$. For $Q \ll Q_c$, the corner flow dominates, and the pressure gradient varies linearly with Q. A transition at such low flow rates is unexpected and partly explains the complex rheology of foam flow in porous media.

1. Introduction

A Newtonian liquid flowing in a straight capillary obeys a linear pressure–velocity relation, independent of capillary geometry. When a long bubble is inserted into the capillary, the relation becomes nonlinear if the capillary is circular (Bretherton 1961). In this paper, we show that for a polygonal capillary the relation can be linear or nonlinear depending on the liquid flow rate and the length of the bubble.

In a circular capillary, a long bubble acts as a tight-fit piston. Because the liquid film lubricating the bubble is thin ($\sim Ca^{2/3}$), dissipation of mechanical energy in the film is an order higher than that in the bulk. Bretherton (1961) has shown the pressure needed to move a long bubble scales as $Ca^{2/3}$. This $\frac{2}{3}$ scaling also applies to a column of liquid

† Present address: The Levich Institute, The City College of CUNY, New York, NY 10031, USA.

containing the bubble because the pressure loss in the bulk liquid is $O(Ca)$, and because the liquid and the bubble move at roughly the same velocity.

In a polygonal capillary, a long bubble acts as a leaky piston (figure 1). The leaky corners have the same order of cross-sectional area as the capillary. Thus, the liquid can either push the bubble (plug flow) or bypass the bubble through corner channels (corner flow). The plug flow obeys the pressure–velocity relation of the bubble because the pressure work driving the plug flow is dissipated predominantly by the liquid films lubricating the bubble, as in circular capillaries. Sections 2–4 determine that the pressure needed to drive a long bubble scales as $Ca^{2/3}$. The same scaling therefore holds for plug flow. Corner flow, however, obeys a linear pressure–velocity relation because the flow is approximately unidirectional (§5). A composite expression valid for both flows is derived in §6, and shows that for a given bubble the corner flow dominates at extremely low flow rates. Application of the linear regime to form flow is discussed in §6.

An integral method is used in this work to determine the fluid pressure needed to move a long bubble at a given velocity. This method differs from the matched-asymptotics method used in calculating the pressure in circular tubes by Bretherton (1961). In that method, the zero-order outer solution with $Ca = 0$ yields the shape of the static bubble. The first-order inner solution determines the profile of the fluid film deposited by the bubble because, in the limit $Ca \to 0$, viscous forces in the film are comparable with capillary forces. Matching the inner and outer solutions gives the curvature of the first-order outer solution. The curvature is then equated to a pressure jump across the interface. In this way, Bretherton established that the pressure drop needed to move a long bubble scales as $Ca^{2/3}$.

In the integral method, the fluid pressure drop is shown to balance the drag of the bubble, which is the shear force exerted by the wall on the fluid films surrounding the bubble. The force balance is described in §2. Section 3 evaluates the drag using the fluid-film results derived in Part 1 (Wong, Radke & Morris 1995). Section 4 calculates the pressure drop. In the method of matched asymptotic expansions, the curvature of the first-order outer solution must be determined subject to the matching conditions. This is an exceedingly difficult task for non-axisymmetric capillaries. In the integral method, the pressure drop is found without using the first-order outer curvature. Thus, the integral method is simpler and better illustrates the physics of the problem.

Figure 1 shows that a strongly non-wetting bubble in a polygonal capillary does not invade the corners. The reduced contact between the bubble and the capillary wall suggests that the drag of a bubble is less in a polygonal capillary than in a circular capillary. Thus, it should be easier to drive a long bubble through a polygonal capillary. However, results of Ratulowski & Chang (1989), which is the only published work related to the present problem, indicate the opposite. They computed the pressure drop of a long bubble in a square capillary. By assuming that the resistance to bubble motion arises from liquid-filled corners, they obtained approximate solutions for $Ca > 3 \times 10^{-3}$ indicating that the pressure drop is larger in a square capillary. We find that the drag originates from liquid films and not from liquid-filled corners. We study six capillary shapes, including regular polygons of 3, 4 and 6 sides and rectangles with aspect ratios 1.2, 1.5 and 2. The results show that the pressure drop in these capillaries is about a third that in the circular capillary, agreeing with the above physical argument.

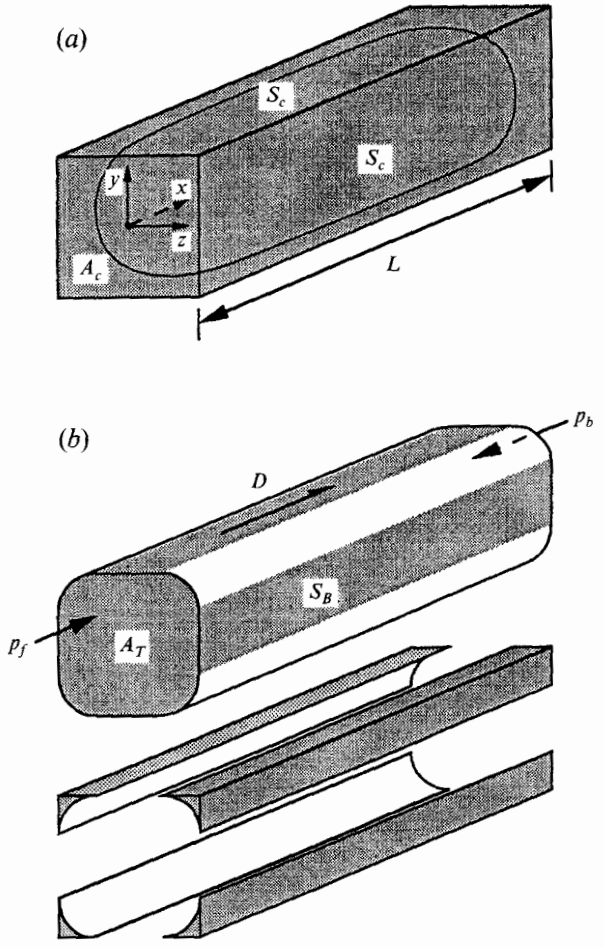

FIGURE 1. Control volumes. (*a*) shows the control volume for a bubble of length L flowing through a wetting liquid in a square capillary. A_c is the cross-sectional area of the capillary, and S_c is the area of the sides. A Cartesian coordinate system is attached to the nose of the bubble. (*b*) shows the divided control volumes. The centre control volume contains the bubble. The driving force $(p_b - p_f)A_T$ balances the drag D acting on the plane sides S_B. The corner control volumes are filled with liquid. The dividing surface (unshaded) has negligible shear force acting on it.

2. Integral force balance

A square capillary demonstrates the force balance. Given a long bubble of length L, the control volume is defined as a square column of length L that encloses the bubble and its surrounding liquid, as shown in figure 1. The control volume moves with the bubble, so the flow is steady in this moving reference frame. A Cartesian coordinate system is fixed at the nose of the bubble with x pointing downstream.

In the force balance, body forces such as gravity and inertia are negligible compared with surface forces, owing to the small size of the capillary. In addition, only streamwise surface forces are needed for determination of pressure–velocity relations. There are two types of surface force acting on the control volume: the shear force on the sides, and the normal force on the ends. A force balance demands that they be equal:

$$\iint_{S_c} Ca \frac{\partial u}{\partial m} \mathrm{d}A = \iint_{A_c} [p(x = L) - p(x = 0)] \mathrm{d}A, \tag{2.1}$$

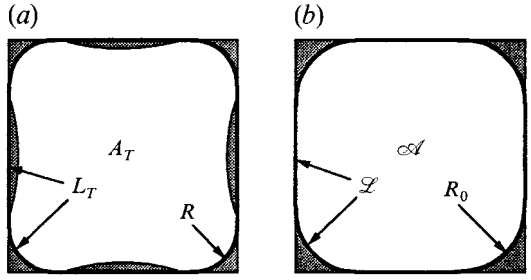

FIGURE 2. Cross-sections of bubbles in a square capillary. (*a*) A cross-section near the front end of a moving long bubble. The thick line defines a centre region that consists of the bubble (clear) and the surrounding liquid films (shaded). A_T is the area of the centre region, and L_T its perimeter. R is the radius of the corner interface. The thickness of the films is exaggerated. (*b*) The two-dimensional interface at the middle of a static non-wetting long bubble. The cross-sectional area of the bubble is $\mathscr{A}$, which has perimeter $\mathscr{L}$. R_0 is the radius of circular-arc meniscus.

Capillary shapes	C_f	C_D			$C_D/\mathscr{A}$		
		$L \ll Ca^{-1}$	$L = Ca^{-1}$	$L = Ca^{-5/3}$	$L \ll Ca^{-1}$	$L = Ca^{-1}$	$L = Ca^{-5/3}$
$N = 3$	12.44	16.07	16.09	21.66	3.536	3.541	4.765
$N = 4$	10.34	13.35	13.38	20.22	3.553	3.559	5.380
$N = 6$	9.329	12.05	12.07	20.27	3.565	3.570	5.998
$B = 1.2$	11.55	14.92	14.94	22.27	3.305	3.311	4.933
$B = 1.5$	13.85	17.89	17.94	25.55	3.163	3.172	4.517
$B = 2$	18.48	23.87	23.98	31.08	3.151	3.165	4.103
Circular	24.37	31.47	31.47	31.47	10.02	10.02	10.02
Slot	7.756	10.02	10.02	10.02	5.009	5.009	5.009

TABLE 1. Coefficients of drag and pressure drop

where u is the x-component of fluid velocity, $\partial/\partial m$ is the outward normal derivative, S_c represents the side area, and A_c is the end area. Throughout this paper, all parameters are made dimensionless by the radius of the largest inscribed sphere a, the surface tension σ, and the bubble velocity U, unless stated otherwise. Because the bubble is long ($L \gg 1$), the pressure difference in (2.1) is an order larger than the normal viscous stresses at the end planes. Hence, the normal viscous stresses are neglected in the force balance. Similarly, variation in fluid pressure over each end plane is small compared with the pressure difference. Hence, the pressure is taken as uniform at the ends:

$$p(x = 0) = p_f, \quad p(x = L) = p_b. \tag{2.2a, b}$$

Thus, (2.1) becomes

$$\iint_{S_c} Ca \frac{\partial u}{\partial m} \mathrm{d}A = (p_b - p_f) A_c. \tag{2.3}$$

The pressure force drives both the bubble and the liquid. The shear force also acts on both. However, by dividing the control volume into a bubble and a liquid region, it is possible to determine the forces that act only on the bubble or the liquid.

Figure 1(*b*) shows how the control volume is divided. The centre control volume contains the bubble, whereas the corner control volumes are filled with liquid. The dividing surface has negligible shear force acting on it. The long central portion of the dividing surface coincides with the bubble surface, and is therefore free of shear force. The ends of the dividing surface cut through the flowing liquid. However, the contact-

line equation (3.2) in Part 1 shows that the ends are of length $O(1)$, which are much shorter than the length of the bubble. Thus, the shear force acting on the dividing surface is small compared with the forces in (2.3). Thus, when (2.3) is applied to the divided control volumes, the pressure force on each control volume must balance the shear force on that control volume.

The centre control volume yields the relation of pressure drop versus bubble velocity. A force balance on the centre control volume requires (figure 1*b*)

$$\iint_{S_B} Ca\frac{\partial u}{\partial m}\mathrm{d}A = (p_b - p_f)\,A_T, \tag{2.4}$$

where S_B represents the plane sides of the control volume (figure 1*b*), and A_T is the projected area of the bubble and fluid films (figure 2*a*). The left-hand side of (2.4) is the drag D of the bubble, which is evaluated in §3 using the fluid velocity profiles derived in Part 1. The result gives

$$D \equiv \iint_{S_B} Ca\frac{\partial u}{\partial m}\mathrm{d}A = C_D\,Ca^{2/3}, \tag{2.5}$$

where C_D depends on capillary geometry and bubble length, as shown in table 1. Substitution of (2.5) into (2.4) gives

$$p_b - p_f = \frac{C_D}{A_T}Ca^{2/3}. \tag{2.6}$$

Since $A_T = O(1)$, and since A_T differs only by $O(Ca^{2/3})$ from the cross-sectional area $\mathscr{A}$ of the static bubble depicted in figure 2(*b*) (§5),

$$p_b - p_f = \frac{C_D}{\mathscr{A}}Ca^{2/3}. \tag{2.7}$$

Table 1 lists the values of $C_D/\mathscr{A}$ for various polygonal capillaries. Equation (2.7) holds for the bubble and the liquid plug flow because both move at roughly the same speed (§6).

A force balance on the corner control volumes determines the relation of liquid pressure versus liquid flow in the corners. Since the bubble is long, the corner flow is predominantly unidirectional and, therefore, obeys a linear pressure–velocity relation. This relation is derived in §5.

3. Drag

The drag of a long bubble is the force exerted by capillary wall on the liquid films surrounding the bubble, and is evaluated by integration of the streamwise viscous shear stress over the wall. As the wetting fluid is dragged by the wall into the film, it experiences the largest shear stress just before entering the film. A similar mechanism at the back end of the film generates another peak in the shear stress. Thus, the drag is concentrated at the two ends of a long bubble, so the two ends are treated separately.

3.1. *Front end*

By symmetry, the drag on the front of the bubble requires evaluation only on half a side. We choose the surface at $y = 1$ to demonstrate the calculation. The drag on the chosen surface is

$$D_f = \iint_{S_f} Ca\frac{\partial u}{\partial y}(y = 1)\,\mathrm{d}x\,\mathrm{d}z, \tag{3.1}$$

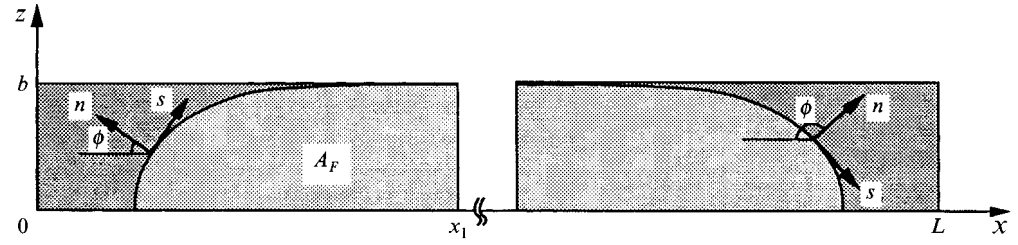

FIGURE 3. Domains of integration at the front and back ends. The rectangular domains are part of the wall surface at $y = 1$. A_F is the area covered by the thin film. n and s are local Cartesian coordinates normal and tangent to the film boundary.

where S_f is the domain $0 \leqslant z \leqslant b$ and $0 \leqslant x \leqslant x_1$ (figure 3), and u is the x-component of fluid velocity. Since the drag arises predominantly from the tip of the film, x_1 is chosen sufficiently far from the front so that any variation of it has no effect on the value of the drag.

The domain of integration S_f can be reduced to the area A_F covered by the film (figure 3) because the shear stress is strongest there. (The precise location of the film is given in Part 1.) Thus,

$$D_f = \int\int_{A_F} Ca \frac{\partial u}{\partial y}(y = 1)\,\mathrm{d}x\,\mathrm{d}z. \tag{3.2}$$

The velocity field in the fluid film is given by (4.5) of Part 1 as

$$Ca\,u = Ca + [h(1-y) - \tfrac{1}{2}(1-y)^2]\frac{\partial(\nabla^2 h)}{\partial x}, \tag{3.3}$$

where h is the film height and $\nabla = \boldsymbol{i}\partial/\partial x + \boldsymbol{k}\partial/\partial z$. Thus, the integrand in (3.2) is

$$Ca\frac{\partial u}{\partial y}(y = 1) = -h\frac{\partial(\nabla^2 h)}{\partial x}. \tag{3.4}$$

This expresses the balance between the x-components of shear and capillary forces acting on a column of base $\partial x \partial z$ and extending from the wall to the interface.

A simple expression for the drag is obtained by converting the area integral in (3.2) into a line integral. First, the integrand in (3.2) is rearranged into a divergence form,

$$Ca\frac{\partial u}{\partial y}(y = 1) = \nabla \cdot \left[\frac{\partial h}{\partial x}\nabla h - \boldsymbol{i}(h\nabla^2 h + \tfrac{1}{2}\nabla h \cdot \nabla h)\right]. \tag{3.5}$$

The divergence theorem is then applied to yield

$$D_f = \oint_{\partial A_F} \left[\frac{\partial h}{\partial x}\nabla h - \boldsymbol{i}(h\nabla^2 h + \tfrac{1}{2}\nabla h \cdot \nabla h)\right] \cdot \boldsymbol{e}\,\mathrm{d}s, \tag{3.6}$$

where $\boldsymbol{e}$ is a unit vector normal to the boundary ∂A_F of the film area A_F, and s is a local Cartesian coordinate tangent to ∂A_F as shown in figure 3.

The line integral in (3.6) has significant values only at the front curved section (figure 3). At the front of the film boundary, Part 1 gives $h \sim Ca^{2/3}$, $n \sim Ca^{1/3}$, $s \sim 1$, and $\boldsymbol{i} \cdot \boldsymbol{e} = -\cos\phi \sim 1$, where n is a local Cartesian coordinate normal to the boundary, and ϕ is the angle between n and the negative x-axis. Thus, the integral along the curved section is $O(Ca^{2/3})$, which is an order larger than the integral along the other two straight sections. The integral along $x = x_1$ is of order $Ca^{4/3}$, because $h \sim Ca^{2/3}$, $z \sim 1$,

and $x \gg 1$. The integral along the symmetry plane $z = 0$ is exactly zero because $\boldsymbol{i}\cdot\boldsymbol{e} = 0$ and $\partial h/\partial x = 0$. Hence, (3.6) simplifies to

$$D_f = \int_C \left[h\frac{\partial^2 h}{\partial n^2} - \frac{1}{2}\left(\frac{\partial h}{\partial n}\right)^2\right]\cos\phi\,\mathrm{d}s, \tag{3.7}$$

where C denotes the curved section of the film boundary with $n \to \infty$. The line integral is further simplified by transforming the independent variable from s to z,

$$D_f = \int_0^b \left[h\frac{\partial^2 h}{\partial n^2} - \frac{1}{2}\left(\frac{\partial h}{\partial n}\right)^2\right]_C \mathrm{d}z. \tag{3.8}$$

Here, b is the half width of the film as shown in figure 3.

The integrand in (3.8) has been determined in Part 1, Appendix B as

$$\left[h\frac{\partial^2 h}{\partial n^2} - \frac{1}{2}\left(\frac{\partial h}{\partial n}\right)^2\right]_C \to k_1 k_2 (3Ca\cos\phi)^{2/3} \quad \text{as } n \to \infty, \tag{3.9}$$

where $k_1 = 0.64304$ and $k_2 = 2.8996$. The angle $\phi = \phi(z)$ is found from the static contact line, which differs from the location of the film boundary only by order $Ca^{1/3}$ in the limit $Ca \to 0$ (Ruschak & Sriven 1977). The contact-line equation (3.2) in Part 1 gives

$$\cos\phi = \left[1 + \left(\frac{\pi}{2bc}\right)^2 \tan^2\left(\frac{\pi z}{2b}\right)\right]^{-1/2}, \tag{3.10}$$

where c is a fitting constant that governs the shape of the contact line. Table 1 in Part 1 lists analytic solutions of b and numerical solutions of c for various polygonal capillaries.

The drag on the basic unit of symmetry (shown in figure 3) follows by substituting (3.9) and (3.10) into (3.8):

$$D_f = k_1 k_2 (3Ca)^{2/3} \int_0^b \left[1 + \left(\frac{\pi}{2bc}\right)^2 \tan^2\left(\frac{\pi z}{2b}\right)\right]^{-1/3} \mathrm{d}z. \tag{3.11}$$

k_1, k_2, and Ca are intrinsic to the motion of the bubble, whereas the integral depends only on the geometry of the contact line. This equation can be applied easily to other menisci in motion, once the shape of the contact line is known.

Equation (3.11) shows clearly that the drag-velocity scaling is a characteristic of the motion of the bubble and is independent of capillary geometry. The same conclusion holds for the back of the bubble, as shown below.

3.2. *Back end*

The drag at the back of a long bubble in a polygonal capillary is qualitatively different from that at the front. Figure 3 shows the rectangular domain at $y = 1$ where the drag is evaluated. Following the procedures for the front, we obtain

$$D_b = \int\int Ca\frac{\partial u}{\partial y}(y = 1)\,\mathrm{d}x\,\mathrm{d}z = \int_C \left[h\frac{\partial^2 h}{\partial n^2} - \frac{1}{2}\left(\frac{\partial h}{\partial n}\right)^2\right]\cos\phi\,\mathrm{d}s. \tag{3.12}$$

Here, C denotes the curved part of the film boundary asymptotically far from the film. The independent variable is then converted from s to z,

$$D_b = -\int_0^b \left[h\frac{\partial^2 h}{\partial n^2} - \frac{1}{2}\left(\frac{\partial h}{\partial n}\right)^2\right]_C \mathrm{d}z. \tag{3.13}$$

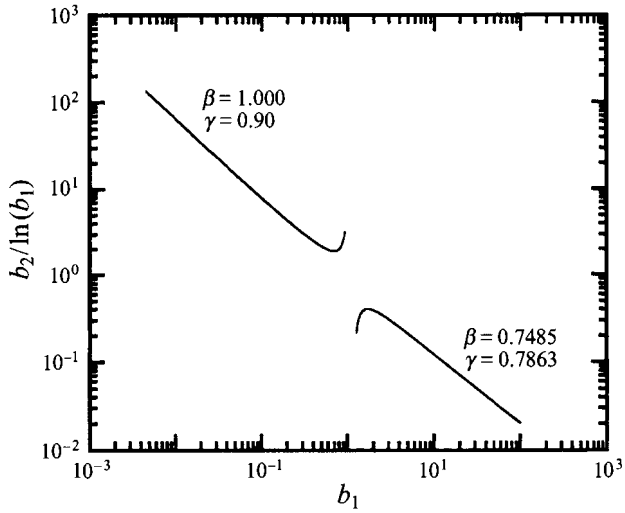

FIGURE 4. Asymptotic behaviour of the numerically determined function $b_2(b_1)$. $b_2/\ln(b_1)$ is plotted against b_1 to better illustrate the functional form in (3.17). The constants β and γ at the zero limit are determined by fitting the numerical solution with $b_1 < 0.2$. The numerical solution with $b_1 > 5$ is used to find the constants for the infinite limit.

This expression differs in sign from (3.8) because, here, s increases as z decreases. The integrand in (3.13) is given in Part 1, Appendix B as

$$\left[h\frac{\partial^2 h}{\partial n^2} - \frac{1}{2}\left(\frac{\partial h}{\partial n}\right)^2\right]_C \to \alpha h_1 b_2 \quad \text{as } n \to \infty, \tag{3.14}$$

where α is the mean curvature of the static bubble and $h_1 = h_1(z)$ is the film height arriving at the back end. b_2 is a numerically determined function of b_1 as shown in figure 9 of Part 1, where

$$b_1 = \frac{\alpha h_1}{[3Ca\cos(\pi - \phi)]^{2/3}}. \tag{3.15}$$

The drag on the basic unit of symmetry (shown in figure 3) is

$$D_b = -\alpha \int_0^b h_1 b_2 \, dz. \tag{3.16}$$

The drag is a function of bubble length L because h_1 depends on L. Part 1 establishes that, for $L \sim Ca^{-5/3}$ or less, $h_1 \sim Ca^{2/3}$. Thus, $b_1 \sim 1$, so $b_2 \sim 1$ (by figure 9 of Part 1). Equation (3.14) then gives $D_b \sim Ca^{2/3}$. Figure 10 of Part 1 shows the integrand $h_1 b_2$ as a function of z for $L \ll Ca^{-1}$, $L = Ca^{-1}$, and $L = Ca^{-5/3}$ and for two different capillary sides. The results show that the maximum of $h_1 b_2$ need not be located at the centre of the film. Table 1 shows that the drag increases with L for $L \leqslant Ca^{-5/3}$.

It is interesting to know if the drag would increase indefinitely with L because the limit $L \to \infty$ or $h_1 = 0$ gives rise to a moving contact line with unbounded drag (Dussan V. 1979). The limit $h_1 \to 0$ corresponds, according to (3.15), to $b_1 \to 0$. From the numerical solution of $b_2(b_1)$, we find

$$b_2 \to \beta b_1^{-\gamma} \ln(b_1) \quad \text{as } b_1 \to 0, \tag{3.17}$$

where $\beta = 1.000$ and $\gamma = 0.90$ are determined by fitting. In figure 4, $b_2/\ln(b_1)$ is plotted against b_1 to show the power-law behaviour. Substitution of (3.17) into (3.16) gives $D_b \to 0$ as $b_1 \to 0$. Thus, the drag vanishes as $h_1 \to 0$ or $L \to \infty$, so the limit is singular.

(In the other limit of $h_1 \to \infty$ or $b_1 \to \infty$, figure 4 shows that b_2 again obeys the functional form in (3.17), but with $\beta = 0.7485$ and $\gamma = 0.7863$. In this limit, $D_b \to -\infty$.)

In contrast to the front of the bubble, the drag at the back depends on the film thickness h_1 and the static curvature α. While the drag at the front is always proportional to $Ca^{2/3}$, the drag at the back can be zero or infinite depending on the incoming film thickness. These differences become apparent in polygonal capillaries because of film rearrangement. In a circular capillary, the fluid film does not rearrange. Hence, the drag at the back reduces to a simple form that conceals the differences.

3.3. *Full bubble*

The drag D of a long bubble is the sum of the drag at the front and back ends:

$$\bar{D}_f = 2ND_f \equiv C_f Ca^{2/3}, \tag{3.18}$$

$$\bar{D}_b = 2ND_b \equiv C_b Ca^{2/3}, \tag{3.19}$$

$$D = \bar{D}_f + \bar{D}_b = C_D Ca^{2/3}. \tag{3.20}$$

Here N is the number of sides of the polygon. Values of C_f and C_D are listed in table 1 for capillary shapes of an equilateral triangle ($N = 3$), a square ($N = 4$), and a regular hexagon ($N = 6$) and for $L \ll Ca^{-1}$, $L = Ca^{-1}$, and $L = Ca^{-5/3}$.

The basic unit of symmetry of a rectangular capillary is a quadrant of the rectangle. The drag from the unity side is different from the side with length B because the contact lines are different. Therefore, (3.11) and (3.16) must be applied individually to each wall. Values of C_f and C_D are also listed in table 1 for rectangular capillaries with aspect ratios $B = 1.2$, 1.5 and 2.0 and for $L \ll Ca^{-1}$, $L = Ca^{-1}$, and $L = Ca^{-5/3}$.

The drag of a long bubble is proportional to $Ca^{2/3}$, independent of bubble length. Section 3.2 shows that the drag at the back of the bubble depends weakly on the length of the bubble: $D_b = O(Ca^{2/3})$ for $L \leqslant O(Ca^{-5/3})$, and $D_b = o(Ca^{2/3})$ for $L \gg Ca^{-5/3}$. However, because the maximium $D_b = O(Ca^{2/3})$ and because the drag (D_f) at the front is $O(Ca^{2/3})$, the total drag $D \sim Ca^{2/3}$, independent of bubble length.

For comparison, we also calculate the drag of long bubbles in circular capillaries and slots. In a circular capillary the contact line is normal to the flow, so $\cos\phi = 1$. In addition, the deposited film does not rearrange, i.e. $h_1 = h_0 = k_1(3Ca)^{2/3}/\alpha$. This gives $b_1 = k_1$ and $b_2 = b_2(k_1) = -0.84529$, independent of bubble length. Thus, for a circular capillary of unit radius, (3.11) and (3.16) require

$$\bar{D}_f = 2\pi k_1 k_2 (3Ca)^{2/3} \equiv C_f Ca^{2/3}, \tag{3.21}$$

$$\bar{D}_b = -2\pi k_1 b_2 (3Ca)^{2/3} \equiv C_b Ca^{2/3}. \tag{3.22}$$

For a slot of height 2, the drag per unit slot width at the front and back of the bubble is

$$\bar{D}_f = 2k_1 k_2 (3Ca)^{2/3} \equiv C_f Ca^{2/3}, \tag{3.23}$$

$$\bar{D}_b = -2k_1 b_2 (3Ca)^{2/3} \equiv C_b Ca^{2/3}. \tag{3.24}$$

As before, the total drag of the bubble is

$$D = \bar{D}_f + \bar{D}_b = C_D Ca^{2/3}. \tag{3.25}$$

Table 1 lists the values of C_f and C_D for comparison. These results show that the drag–velocity scaling is independent of capillary geometry.

4. Fluid pressure drop

Fluid pressure at the back of a flowing bubble is higher than that at the front, and the difference balances the drag. This balance is given by (2.7) as

$$p_b - p_f = \frac{C_D}{\mathscr{A}} Ca^{2/3}, \tag{4.1}$$

where $\mathscr{A}$ is the cross-sectional area of the static bubble determined by Wong, Morris & Radke (1992). Values of $C_D/\mathscr{A}$ are listed in table 1 for different capillaries. (Our value for a circular capillary differs slightly from that of Bretherton (1961) because his solution of $b_2(k_1)$ is off by 14%.) We observe that the pressure drop in six different polygonal capillaries for $L \leqslant Ca^{-1}$ is roughly the same and is about a third that in the circular capillary. The pressure–velocity scaling law is thus insensitive to capillary geometry.

The integral method that calculates the fluid pressure drop across a long bubble also applies to the bubble front or back individually. As shown in the Appendix, an integral force balance on the front end of a long bubble gives

$$p_f = -\alpha - \frac{C_f}{\mathscr{A}} Ca^{2/3}, \tag{4.2}$$

where the fluid pressure p_f is gauged relative to the gas pressure (which is set to zero), and α is the mean curvature of the static bubble. Substitution of (4.2) into (4.1) gives the fluid pressure at the back end:

$$p_b = -\alpha + \frac{C_b}{\mathscr{A}} Ca^{2/3}. \tag{4.3}$$

These end pressures apply to finite as well as semi-infinite bubbles. Moreover, they show that the first-order change in bubble shape is $O(Ca^{2/3})$. We have also determined the end pressures by the method of matched asymptotic expansions and arrived at the same solution (Wong 1992, p. 196). Nevertheless, we find that the integral method is simpler and illustrates better the physics of the problem.

5. Fluid flow

A long bubble in a circular tube acts as a tight-fit piston. Therefore, the bubble and fluid move at roughly the same speed (Bretherton 1961). A long bubble in a polygonal tube, however, behaves like a leaky piston. The fluid prefers to bypass the bubble through the leaky corners because of the large drag of the bubble. For moderately long bubbles, the corner flow is an order faster than the bubble. This leading contribution to fluid flow is missing in circular capillaries. Thus, polygonal capillaries display certain foam flow behaviours that cannot be explained using circular-tube models.

Fluid flow in the corner control volume (shown in figure 1*b*) is predominantly unidirectional. As shown in figure 1(*a*), a long bubble has an extended middle section where the cross-sectional area of the bubble remains essentially constant. The end regions where the area varies significantly are of length order one because the three-dimensional end meniscus approaches the two-dimensional corner meniscus exponentially (see (3.2) of Part 1). Away from the ends, the area of the fluid-filled corners varies by order $Ca^{2/3}$ because the capillary pressure varies by that order as indicated by (4.2) and (4.3). Since the corner area is $O(1)$, the variation in area is negligible. Thus,

Capillary shapes	κ	c_1†	c_2
$N=3$	6.623×10^{-3}	4.506×10^{-3}	0.87486
$N=4$	7.220×10^{-4}	6.415×10^{-4}	0.93968
$N=6$	5.011×10^{-5}	5.157×10^{-5}	0.97557
$B=1.2$	1.020×10^{-3}	7.025×10^{-4}	0.94024
$B=1.5$	1.482×10^{-3}	7.812×10^{-4}	0.94239
$B=2$	2.218×10^{-3}	8.737×10^{-4}	0.94713

† For $L \ll Ca^{-1}$.

TABLE 2. Flow constants

fluid flow in the corner control volume is taken as unidirectional. In such cases, an integral force balance is unnecessary because for unidirectional flows the pressure gradient is constant and is related to the non-dimensional volume flux Q_1 by

$$Q_1 = \frac{\kappa}{Ca}\left(-\frac{dp}{dx}\right), \tag{5.1}$$

where κ is a constant that depends only on corner geometry. Unidirectional flows along corners bounded by a wedged wall and a circular-arc meniscus have been studied by Ransohoff & Radke (1988). Their solutions, rearranged into the form of (5.1), give the values of κ in table 2 for different polygonal capillaries. The pressure gradient is taken as $(p_b-p_f)/L$ (figure 1). Thus,

$$Q_1 = -\frac{\kappa}{Ca\,L}(p_b-p_f). \tag{5.2}$$

The pressure drop is then eliminated using (4.1),

$$Q_1 = -\frac{\kappa C_D}{\mathscr{A}L}Ca^{-1/3}. \tag{5.3}$$

Q_1 represents a ratio of corner-flow velocity to bubble velocity because Q_1 was made dimensionless by a^2U. Thus, (5.3) shows that the corner flow is an order faster than the bubble. The negative sign indicates that the flow is in the opposite direction to x and in the same direction as the bubble.

Beside corner flow, the fluid also flows by pushing the bubble, which acts as a (leaky) piston. The plug flow so generated equals the velocity of the bubble multiplied by the cross-sectional area of the bubble, i.e.

$$Q_2 = -\mathscr{A}, \tag{5.4}$$

where, as before, $\mathscr{A}$ is the area of the static bubble.

The sum of corner flow and plug flow gives the total fluid flow Q_T,

$$Q_T = |Q_1+Q_2|. \tag{5.5}$$

By dividing Q_T by the capillary area A_c, an average fluid velocity is obtained as

$$V = \frac{c_1}{L}Ca^{-1/3}+c_2. \tag{5.6}$$

Values of c_1 and c_2 for various capillaries are listed in table 2. The constant

$c_1 = \kappa C_D/\mathscr{A}A_c$ is calculated using the value of C_D corresponding to $L \ll Ca^{-1}$. Other values of C_D for $L \geqslant O(Ca^{-1})$ are not needed because when $L \gg Ca^{-1/3}$ the corner flow is already negligible compared with the plug flow.

The corner and plug flows in (5.6) are listed in descending powers of Ca. However, either flow can dominate because the bubble length L is arbitrary. When $L \gg Ca^{-1/3}$, (5.6) gives $V = c_2 (= \mathscr{A}/A_c)$. Thus, when a bubble is very long or semi-infinite, the average fluid velocity is the volume flow rate of the moving bubble divided by the area of the capillary. Table 2 shows that $c_2 \sim 1$ for polygonal capillaries. For circular capillaries, $c_2 = 1$.

When $1 \ll L \ll Ca^{-1/3}$, (5.6) gives $V = c_1 L^{-1} Ca^{-1/3}$. In the limit $Ca \to 0$, $V \gg 1$, so the liquid moves much faster than the bubble. In this case, two bubbles of lengths L_1 and L_2 and velocities U_1 and U_2, when driven by the same liquid flow, obey

$$\frac{U_1}{U_2} = \left(\frac{L_1}{L_2}\right)^{3/2}. \tag{5.7}$$

Thus, longer bubbles move faster, because the resistance to the corner flow is higher. This bubble-length dependence is a consequence of corner flow and is absent in circular capillaries.

The case of $1 \ll L \ll Ca^{-1/3}$ is relevant to foam flow because foam bubbles are only moderately long. In this case, (5.6) shows that the corner flow dominates as $Ca \to 0$. However, because $c_1 \ll 1$ (table 2), the corner flow is small compared with the plug flow at $Ca \sim 10^{-6}$, which is a typical value encountered in foam-flow experiments. Even smaller capillary numbers are needed to see the corner-flow effects. Transition at such small Ca is unexpected and explains certain peculiar foam behaviours as discussed in the next section.

6. Fluid pressure versus fluid flow

The gradient in fluid pressure varies linearly with fluid flow in one range of flow rate and varies nonlinearly in another range. This behaviour appears only in polygonal capillaries and is important in understanding foam flow in porous media. Let $Q = CaQ_T$ be the liquid flow rate made dimensionless by $\sigma a^2/\mu$. (Q can be thought of as a capillary number based on liquid velocity.)

The liquid flow is the sum of corner flow and plug flow:

$$Q = |CaQ_1 + CaQ_2| \tag{6.1}$$

The pressure–velocity relation of corner flow is given by (5.2) as

$$CaQ_1 = \kappa\left(\frac{p_b - p_f}{L}\right). \tag{6.2}$$

The pressure–velocity relation of plug flow is found from (4.1) with the bubble velocity replaced by the liquid velocity in (5.4):

$$CaQ_2 = -\frac{\mathscr{A}^{5/2}}{C_D^{3/2}}(p_b - p_f)^{3/2}. \tag{6.3}$$

Substitution of (6.2) and (6.3) into (6.1) gives

$$Q = \kappa\left[1 + \frac{\mathscr{A}^{5/2} L}{C_D^{3/2}\kappa}(p_b - p_f)^{1/2}\right]\left(\frac{p_b - p_f}{L}\right). \tag{6.4}$$

In experiments, the flow rate is usually the independent variable. An accurate inversion of (6.4) follows when the plug-flow term inside the brackets is expressed in terms of Q using the plug-flow limit of (6.4):

$$\frac{p_b - p_f}{L} = \frac{Q/\kappa}{1+(Q/Q_c)^{1/3}}, \tag{6.5a}$$

where

$$Q_c = \frac{1}{\mathscr{A}^5}\left(\frac{\kappa C_D}{L}\right)^3 \tag{6.5b}$$

is a critical volume flux that marks the transition from one regime to another. Equation (6.5*b*) shows that Q_c depends strongly on the bubble length L and the capillary shape (κ). For the six polygonal capillaries studied, $Q_c \ll 10^{-6}$ because $L \gg 1$ and $\kappa < 10^{-2}$ (table 2). For $Q \ll Q_c$, (6.5*a*) gives

$$\frac{p_b - p_f}{L} \sim Q. \tag{6.6}$$

This is the corner-flow regime where the pressure work is dissipated by fluid motion in the corners. For $1 \gg Q \gg Q_c$,

$$\frac{p_b - p_f}{L} \sim Q^{2/3}. \tag{6.7}$$

This is the plug-flow regime where dissipation is strongest at the two ends of the deposited fluid films. The nonlinear relation also holds for circular tubes. However, the linear regime and the transition at extremely low capillary numbers can only be demonstrated by polygonal capillaries. Application of these results to foam flow is discussed below.

In some foam-flow experiments, the pressure drop over a porous core varies linearly with liquid flow, but is rather independent of gas flow (Kovscek & Radke, 1994; and references therein). In some other experiments, the pressure drop varies nonlinearly with liquid or gas flow (e.g. Ali, Burley & Nutt 1985). The nonlinear behaviour has been explained using the nonlinear response of bubble flow in circular tubes, but none of the existing theory can predict the linear regime. We calculate the capillary number (Q) using the reported liquid velocities, and find that the first set of experiments was usually done at extremely low capillary numbers ($\sim 10^{-8}$), but in the second $Q \sim 10^{-5}$. This work shows that at extremely low capillary numbers ($Q \ll Q_c$), the pressure gradient varies linearly with liquid flow. Further, the bubble motion dissipates an insignificant amount of mechanical energy, and therefore has no effect on the pressure gradient. As the capillary number increases ($Q \gg Q_c$), the pressure–velocity relation for either the liquid or the bubble becomes nonlinear. These results provide a simple explanation for the complex foam behaviour.

7. Conclusions

The fluid pressure drop needed to move a long bubble in a polygonal capillary scales as $Ca^{2/3}$. The proportionality constant for six different polygonal capillaries is about a third that for the circular capillary. Thus, the scaling relation of pressure drop versus bubble velocity is insensitive to capillary geometry.

An integral method is adapted here to calculate the pressure drop. This approach is simpler than the method of matched asymptotic expansions because it does not require

the curvature of the first-order outer solution. In the integral method, the pressure drop is shown to balance the drag, which is determined by the films at the two ends of the bubble. Simple expressions have been obtained for the drag at both ends that can be easily applied to other moving menisci. Because the drag arises from thin films, capillary corners have no effect on the scaling relation between fluid pressure drop and bubble velocity.

However, the physics of bubble flow is best illustrated by the relation of liquid pressure gradient versus liquid flow. In a polygonal capillary, the relation can be linear or nonlinear depending on the liquid flow rate Q. The transition occurs at a critical flow rate Q_c, whose value depends strongly on capillary geometry and bubble length. For the six polygonal capillaries studied, $Q_c \ll 10^{-6}$. For $1 \gg Q \gg Q_c$, the gradient in liquid pressure varies with $Q^{2/3}$. For $Q \ll Q_c$, the pressure gradient varies linearly with Q. The linear regime is a result of corner flow and is therefore absent in circular capillaries. This linear regime is able to explain the observation in foam-flow experiments that, at extremely low flow rates, the pressure gradient varies linearly with liquid flow, but is independent of gas flow.

This work was partially supported by NSF Grant EAR8610494 and by the Assistant Secretary for Fossil Energy, Office of Oil, Gas, and Shale Technologies of the United States Department of Energy under Contract DE-AC03-76SF00098 to the Lawrence Berkeley Laboratory of the University of California. H.W. acknowledges fellowship support from University of California, Berkeley during this work.

Appendix. Dynamic pressure jump across the bubble front

The fluid pressure drop across a long bubble is derived in §2 by a balance of forces on the whole bubble. Here, the fluid pressure at the front of the bubble is determined by a similar force balance on only the front end. Figure 5 shows the control volume of the force balance. There are three kinds of surface forces acting on the control volume: the pressure forces on the end planes at $x = 0$ and $x = x_1$, the surface tension force on the end plane at $x = x_1$, and the viscous shear force on the four sides of the square column.

In the limit $Ca \to 0$, the force balance simplifies. First, the fluid pressure in the corners at $x = x_1$ is taken as the constant fluid pressure p_f at $x = 0$. This is possible because variation in fluid pressure is of order $Ca^{2/3}L^{-1}$, which is much smaller than the quantities that we are interested in. Secondly, the pressure force exerted on the fluid films at $x = x_1$ is of order $Ca^{4/3}$ (see Part 1), and is negligible in the force balance. Remaining terms in the force balance include the pressure force $p_f A_T$, the surface tension force L_σ, and the viscous shear force or the drag $\bar{D}_f$:

$$p_f A_T = -L_\sigma - \bar{D}_f, \tag{A 1}$$

where A_T is the sum of the areas of the bubble and fluid films (figure 2*a*), L_σ is the length of the interface at $x = x_1$, and $\bar{D}_f = C_f Ca^{2/3}$ is the drag at the front end given in §3.3. Dividing (A 1) by A_T yields

$$p_f = -\frac{L_\sigma}{A_T} - \frac{C_f}{\mathscr{A}} Ca^{2/3}, \tag{A 2}$$

where A_T in the smallest term has been replaced by the cross-sectional area $\mathscr{A}$ of the static bubble since they differ only by $O(Ca^{2/3})$. When $Ca = 0$, the static solution states that $p_f = -\alpha$, where α is the mean curvature of the static bubble (Wong *et al.* 1992).

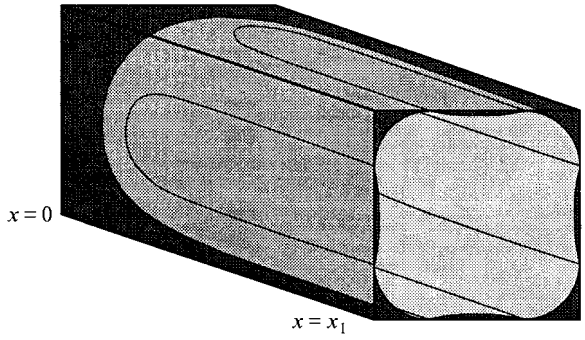

FIGURE 5. Schematic of the control volume on the front end of a long bubble (light shading) flowing through a wetting liquid (dark shading) in a square capillary. x_1 is chosen sufficiently far from the front such that its location has no effect on the force balance.

The rest of this Appendix is devoted to the proof of $L_\sigma/A_T = \alpha + O(Ca^{4/3})$. The result gives the two leading terms of the fluid pressure as

$$p_f = -\alpha - \frac{C_f}{\mathscr{A}} Ca^{2/3}. \tag{A 3}$$

The proof consists of two steps. First, we show that $L_\sigma = L_T + O(Ca^{4/3})$ where L_T is the perimeter of A_T as illustrated in figure 2(*a*). The two perimeters L_σ and L_T differ by the excess length of the film surface as compared with the length of capillary sidewalls covered by the films. The slope of the films has been determined in Part 1 as order $Ca^{2/3}$. This gives an excess length of order $Ca^{4/3}$. Therefore,

$$\frac{L_\sigma}{A_T} = \frac{L_T}{A_T} + O(Ca^{4/3}). \tag{A 4}$$

Hence, to the leading order, L_σ/L_T is the ratio of perimeter to area for the area A_T.

The second step of the proof shows that the minimum of the ratio L_T/A_T occurs at $Ca = 0$. Since the area A_T is defined by capillary side walls and circular-arc interfaces in the corners, the only parameter that can change A_T is the radius R of the corner interface. The minimum of L_T/A_T is reached at a particular value of R corresponding to the static radius R_0. This is expected because L_T/A_T represents the ratio of area to volume for a two-dimensional meniscus, so the minimum always occurs at equilibrium (Mayer & Stowe 1965). Since the deviation from the minimum must be at least quadratic, we obtain

$$\frac{L_T(R)}{A_T(R)} = \frac{\mathscr{L}}{\mathscr{A}} + O(R - R_0)^2, \tag{A 5}$$

where $\mathscr{L} = L_T(R_0)$ is the perimeter of the cross-sectional area $\mathscr{A}(= A_T(R_0))$ of the static bubble, as shown in figure 2(*b*). Appendix A in Part 1 gives $\mathscr{L}/\mathscr{A} = \alpha$. Since R differs from R_0 by order of $Ca^{2/3}$, (A 4) and (A 5) give

$$\frac{L_\sigma}{A_T} = \alpha + O(Ca^{4/3}). \tag{A 6}$$

This completes the proof.

REFERENCES

ALI, J., BURLEY, R. W. & NUTT, C. W. 1985 Foam enhanced oil recovery from sand packs. *Chem. Engng Res. Des.* **63**, 101–111.

BRETHERTON, F. P. 1961 The motion of long bubbles in tubes. *J. Fluid Mech.* **10**, 166–188.

DUSSAN V., E. B. 1979 On the spreading of liquids on solid surfaces: static and dynamic contact lines. *Ann. Rev. Fluid Mech.* **11**, 371–400.

KOVSCEK, A. R. & RADKE, C. J. 1994 Fundamentals of foam transport in porous media. In *Foams: Fundamentals and Applications* (ed. L. L. Schramm), vol. 242, pp. 115–163. Washington, DC. American Chemical Society.

MAYER, R. P. & STOWE, R. A. 1965 Mercury porosimetry-breakthrough pressure for penetration between packed spheres. *J. Colloid Sci.* **20**, 893–911.

RANSOHOFF, T. C. & RADKE, C. J. 1988 Laminar flow of a wetting liquid along the corners of a predominantly gas-occupied noncircular pore. *J. Colloid Interface Sci.* **121**, 392–401.

RATULOWSKI, J. & CHANG, H. C. 1989 Transport of gas bubbles in capillaries. *Phys. Fluids* A **1**, 1642–1655.

RUSCHAK, K. J. & SCRIVEN, L. E. 1977 Developing flow on a vertical wall. *J. Fluid Mech.* **81**, 305–316.

WONG, H. 1992 The motion of a long bubble in polygonal capillaries at low capillary numbers. PhD thesis, University of California, Berkeley.

WONG, H., MORRIS, S. & RADKE, C. J. 1992 Two-dimensional menisci in non-axisymmetric capillaries. *J. Colloid Interface Sci.* **148**, 284–287.

WONG, H., RADKE, C. J. & MORRIS, S. 1995 The motion of long bubbles in polygonal capillaries. Part 1. Thin films. *J. Fluid Mech.* **292**, 71–94.